Materials Advances

ROYAL SOCIETY OF CHEMISTRY

PAPER

View Article Online
View Journal | View Issue

Cite this: *Mater. Adv.*, 2025, 6, 4817

An excellent photochemical reduction property of Cr(VI) upon visible light illumination in a hydroxyl-functionalized zirconium-based metal–organic framework†

My V. Nguyen, * Vu T. Luu and An T. D. Phan

To design a MOF material with an appropriate band gap value for visible light absorption and a rapid photoreduction rate, a Zr-based MOF modified by hydroxyl groups was successfully fabricated, and its Cr(VI) photoreduction performance was investigated. Subsequently, the experimental data revealed an extraordinary Cr(VI) removal efficiency for HCMUE-2, achieving up to 100% reduction after 90 min under irradiation by visible light at pH = 1. In particular, the complete characterization of the material was confirmed through modern analytical procedures, including powder X-ray diffraction (PXRD), Fourier transform infrared (FT-IR) and Raman spectroscopy, thermogravimetric analysis combined with differential scanning calorimetry (TGA-DSC), scanning electron microscopy incorporating energy-dispersive X-ray (SEM-EDX), UV-vis diffuse reflectance spectroscopy (UV-vis/DRS), and X-ray photoelectron spectroscopy (XPS). Notably, HCMUE-2 retains its Cr(VI) photoreduction percentage for five consecutive cycles without any significant decrease. Additional combined experiments proved that the structural robustness and morphology of the material were maintained after the photocatalytic reduction process. A plausible photoreduction mechanism was elucidated mainly through scavenger capture investigations, showing that regulated electrons are the primary reactive species responsible for converting Cr(VI) into Cr(III) under the identified conditions. These findings illustrate that a Zr-based MOF modified by OH moieties is a promising candidate for the photoreduction of highly toxic Cr(VI) contaminants from wastewater in real-life situations.

Received 3rd April 2025,
Accepted 6th June 2025

DOI: 10.1039/d5ma00319a

rsc.li/materials-advances

1. Introduction

Owing to the rapid growth of technology and industrialization, the accompanying protection issues have received a lot of attention from scientists. Accordingly, many hidden threats have been revealed, including air pollution,[1] soil contamination,[2] and water pollution caused by toxic organic compounds and heavy metal ions, which can be associated with chromium.[3] In fact, the Cr ion exists in an aqueous medium in two oxidation types: hexavalent (Cr(VI)) and trivalent (Cr(III)) states. Cr(VI) ions are known in many species under various pH conditions, such as CrO_4^{2-}, $Cr_2O_7^{2-}$, and $HCrO_4^-$. It is noteworthy that the Cr(VI) ion can seriously damage the cell structures of marine organisms, causing oral toxicity and stomach cancer in humans.[4] Highly toxic Cr(VI) can be accounted for by the rapid movement of Cr(VI) in water.[5] Meanwhile, Cr(III) is less mobile than Cr(VI), leading to less poisoning by Cr(III). Additionally, research proved that a small amount of Cr(III) is beneficial for the supply of trace elements for plants and the human body.[6] Therefore, an effective and economical method for converting Cr(VI) into Cr(II) is urgently needed. According to previous studies, different treatment procedures to eliminate Cr(VI) from wastewater have been explored, including adsorption,[7,8] membranes,[9,10] electrochemistry,[11,12] ion exchange,[13] and photoreduction.[14,15] It should be noted that the photocatalytic reduction method has demonstrated unique performance with high possibility of regeneration, low cost, and high yield in converting Cr(VI) into Cr(III) under visible light, which is less toxic, more eco-friendly, and easily precipitated at neutral pH in the form of $Cr(OH)_3$.[16,17] Over many decades, a variety of photocatalysts have been utilized for purging Cr(VI) in a water environment *via* photoreduction mechanisms, such as TiO_2,[18,19] g-C_3N_4-based nanomaterials,[20] WO_3,[21,22] and their composites/derivatives with TiO_2, including ZnO/TiO_2,[23] NiO/ZnO,[24] and CuS/TiO_2,[25] with promising properties. Nevertheless, their band gap, which plays a vital role in the hole–electron separation rate and reducing ability of the

Faculty of Chemistry, Ho Chi Minh City University of Education, Ho Chi Minh City 700000, Vietnam. E-mail: mynv@hcmue.edu.vn

† Electronic supplementary information (ESI) available: Full characterization and additional measurement details. See DOI: https://doi.org/10.1039/d5ma00319a

material, is approximately 3.0–3.2 eV. These values are inconvenient for taking advantage of available visible light resources to effectively address the direct photocatalytic reduction process of Cr(VI) into Cr(III) from wastewater. Hence, the design of materials showing extraordinary performance, such as a rapid reduction interval, low band gap energy, and high porosity, is necessary to enhance the efficient photoreduction of Cr(VI).

To date, scientists have focused on researching a new family of porous materials, metal–organic frameworks (MOFs), with interesting behavior that allows the stated obstacles to be overcome in converting Cr(VI) from wastewater compared to traditional materials. Specifically, MOFs are constructed from metal clusters containing inorganic nodes and organic linkers, driving unique performances, such as high and adjusted porosity, large specific surface area, and facile modification of the organic linkers by functional groups. This leads to diverse applications in many fields of MOF materials, including gas sensors,[26,27] adsorption,[28–31] energy storage,[32,33] and catalysis.[34–37] Notably, numerous investigations have employed MOF materials as potential semiconductors in the photocatalytic process under UV-vis irradiation with reliable data, demonstrating an appreciated band gap and effective performance. This proves that MOFs are highly promising materials in the photocatalytic field, especially for Cr(VI) reduction.[38–40] Two main factors are revealed that can have a considerable effect on the light absorption range of the MOF material: the nature of the organic linker and the classification of metal nodes within the MOF architecture.[41] Based on recent studies, the correlation between the electron density of functional groups within the linker and the band gap of the MOF materials was exhibited through the functionalization of amino ($-NH_2$) and hydroxyl (–OH) onto a UiO-66 structure. They shift effective harvesting to the absorption range of visible light and improve the photoreduction possibility *via* efficient electron transfer from the linker to the metal clusters.[42,43] Xie *et al.* introduced the hydroxyl moieties onto UiO-66 by modifying the linker and evaluated the effect of the OH groups on the photoreduction of Cr(VI) by the material. As a consequence, UiO-66$(OH)_2$, with two hydroxyl groups, has a much higher photocatalytic ability for Cr(VI) reduction than UiO-66(OH) or unmodified UiO-66.[42] However, the above investigations only looked at the influence of the functional groups on the absorption property of the MOF materials in the visible light region without detailed consideration the adsorption active sites inside the backbone. This is one of the factors that helps boost the Cr(VI) photoreduction process. It can be explained by the adsorption centers helping the Cr(VI) ions to move into the pore channels of the MOF structure where they are rapidly reduced by the available photocatalytic sites, resulting in an increase in the reduction rate and a considerable improvement in reduction efficiency. With this in mind, we propose the synthesis of hydroxyl-functionalized zirconium-based MOFs, with more appropriate pore size and containing a dense distribution of OH groups within the linker and metal-oxo clusters, can remarkably assist the adsorption ability of Cr(VI) *via* the protonation process of hydroxyl moieties inside the backbone in an acidic medium and appreciably enhance visible light absorption through a suitable band gap energy. This is a distinctive approach to surmounting the aforementioned limitations in published reports with respect to the Cr(VI) photocatalytic reduction yield.

In this contribution, a Zr-based MOF was successfully prepared by a solvothermal procedure *via* the modification of hydroxyl moieties onto the MOF architecture, termed HCMUE-2, with an unexpected photoreduction efficiency for Cr(VI). Noteworthily, the complete characterizations of the material and plausible Cr(VI) photocatalytic mechanism were confirmed *via* reliable analyses. Moreover, the fabrication of HCMUE-2 exhibits easy scale-up, relatively low cost, with a low amount of the material being used in photocatalysis, leading to prospective applications in real-life situations. These results show that the hydroxyl-modified Zr-based MOF is a promising material as an excellent photocatalyst for effectively reducing Cr(VI) species from an aqueous medium.

2. Experimental section

2.1. Starting chemicals and methods

The starting materials were obtained from commercial suppliers with high purity, including zirconium oxychloride octahydrate ($ZrOCl_2{\cdot}8H_2O$, 99%), 2,6-naphthalenedicarboxylic acid (H_2NDC, 98%), oleum (SO_3 in concentrated H_2SO_4, 20%), *N*,*N*-dimethylformamide (DMF, 98%), hydrochloric acid (HCl, 37%), formic acid (HCOOH, 85%), acetone (CH_3COCH_3, 99.5%), methanol (MeOH, 99%), 1,5-diphenylcarbazide (1,5-DPC, 98%), silver nitrate ($AgNO_3$, 98%), isopropyl alcohol (IPA, 98%), disodium ethylenediaminetetraacetate (2Na-EDTA, 98%), and *p*-benzoquinone (98%). In particular, 4,8-disulfonaphthalene-2,6-dicarboxylic acid (H_4SNDC) and 4,8-dihydroxynaphthalene-2,6-dicarboxylic acid ($H_2NDC(OH)$) linkers were synthesized *via* a modification process, similar to published investigations,[40,44,45] which are clearly illustrated in Section S1 (ESI†).

Fourier transform infrared spectroscopy (FT-IR) analyses were carried out on an FT/IR-6600 spectrometer (Jasco). Raman spectra were recorded on an XploRA one 532 nm spectrometer (Horiba). Thermogravimetric analysis (TGA) incorporating differential scanning calorimetry (DSC) was conducted on a LabSys Evo 1600 TGA thermal analysis system (SETARAM) in the temperature range of 25–800 °C at a constant heating rate of 10 °C min^{-1} in a dry air medium. ^{1}H-NMR measurement was performed on an AVANCE Neo 600 MHz NMR spectrometer (Bruker). The N_2 adsorption isotherm was conducted on a TriStar II Plus surface characterization analyzer (Micromeritics). A liquid N_2 bath was used for measurements at 77 K. Before N_2 sorption measurements, the sample was activated at 120 °C under vacuum for 1 day. Powder X-ray diffraction (PXRD) data were obtained using an Ni-filtered Cu Kα source (λ = 1.54718 Å) on a D8 Advance diffractometer (Bruker). Scanning electron microscopy (SEM) images were recorded on an FESEM S-4800 microscope (Hitachi) combined with energy-dispersive

X-ray (EDX) spectroscopy and mapping measured using an EDX H-7593 instrument (Horiba). Transmission electron microscopy (TEM) was carried out on a Jeon 1010 microscope (Hitachi). X-ray photoelectron spectroscopy (XPS) was conducted on a PHI 5000 X-ray photoelectron spectrometer (Chigasaki). Liquid UV-vis spectroscopy analyses were determined using a Lambda 25 spectrometer (PerkinElmer). UV-Vis diffuse reflectance spectra were confirmed by employing a V-770 UV-vis spectrophotometer (Jasco) equipped with a diffuse reflectance accessory and using barium sulfate as a reference standard. Cyclic voltammetry analysis was carried out on an MPG-2 electrochemical workstation (Biologic). Accordingly, Na_2SO_4 solution (0.1 M) was employed as an electrolyte. A three-electrode cell was designed with a saturated Ag/AgCl electrode ($E^{ref}_{Ag/AgCl}$ = 0.22 V) as a reference electrode, a counter electrode of a Ti grid, and a modified glassy carbon as a working electrode. Photoluminescence spectroscopy and time-resolved fluorescence spectra were performed on an FLS1000 analyzer (Edinburgh). Photocurrent analyses were conducted on a CIMPS system electrochemical workstation (Zahner). Herein, 5 mg of HCMUE-2 was dispersed in isopropanol (2 mL), then drop coated on a fluorine-doped tin oxide (FTO) plate (1.0 × 1.0 cm) and dried for 2 h at 100 °C. The photocurrent measurements were performed using a three-electrode cell with HCMUE-2 coated onto the FTO electrode as a working electrode in 0.2 M Na_2SO_4 solution, with Ag/AgCl, and Pt electrodes as the reference and counter electrodes, respectively. Atomic absorption spectrophotometry (AAS) was carried out on an iCE 300 Series spectrometer (Thermo Scientific) to quantify Cr ion content with an absorption wavelength of 357.9 nm.

2.2. Synthesis of HCMUE-2

According to a previously reported study,[46] a mixture of $H_2NDC(OH)$ linker (32.7 mg, 0.132 mmol), $ZrOCl_2{\cdot}8H_2O$ salt (39.3 mg, 0.122 mmol), formic acid (1.5 mL), and DMF (6 mL) was introduced into a 20 mL vial and sonicated for 20 min until the precursors were entirely dissolved. The mixture was then heated at 120 °C for 3 days. After that interval, the mixture was cooled to room temperature, centrifuged, and washed with DMF for 2 days (10 mL per day) to decant the unreacted substances. The solid was continuously exchanged with MeOH solvent for 2 days (15 mL per day). Finally, the product was dried and activated under vacuum at 120 °C for 1 day to remove the guest solvents from the MOF architecture and acquire a pure brown powder, denoted HCMUE-2 (88% yield, based on Zr^{4+}).

2.3. Photocatalytic study

The experiments were carried out at room temperature under the illumination of two 50 W white LED lamps (LED BULB PBCD, Paragon) at a constant stirring rate. Specifically, 15 mg of HCMUE-2 was added to a 50 mL glass flask containing 40 mL of Cr(VI) solution (10 mg L^{-1}). The solution pH was controlled from 1 to 5 with HCl solution (1 M). Before illumination, the mixture was stirred in the dark for 60 min to establish adsorption–desorption equilibrium. Through the Cr(VI) photoreduction process, 5 mL samples were withdrawn at 15 min intervals to observe changes in Cr(VI) concentration in the mixture. Each suspension was centrifuged twice to separate the catalyst. The resulting solution was treated using the DPC method, with the complex formed 10 min later in the dark. In detail, 1,5-DPC (250 mg) was dissolved in 100 mL of acetone through ultrasonication to obtain a 0.01 M DPC solution. For analysis, a mixture including 1 mL of DPC solution and 1 mL of 0.5 M H_2SO_4 was introduced into 2 mL of the sample after the various intervals. Notably, this complex possesses limited stability for 15 min. The remaining concentration of Cr(VI) was determined at a maximum absorption wavelength (542 nm) through a calibration curve established from standard solutions (Fig. S3, ESI†). Here, the photoreduction yield (%) of Cr(VI) was confirmed with the following equation:

$$\text{Photoreduction yield (\%)} = \frac{(C_0 - C_t)}{C_0} \times 100 \qquad (1)$$

where C_0 and C_t are the concentrations of Cr(VI) ions in solution at the beginning and at time t, respectively.

2.4. Reusability

Photoreduction cycles were conducted to evaluate the stability of the material in practical applications. Subsequently, the HCMUE-2 sample was treated with 1% HNO_3 solution to remove all traces of Cr^{3+} ions, which had been generated during photocatalysis and adsorbed into the pore channels of the MOF structure. This process was then maintained until the filtration was tested without the presence of traces of Cr^{3+} *via* the UV-vis spectra. Subsequently, the material was collected and washed with water and MeOH until the filtrate reached a neutral pH value. Then, the powder was centrifuged, dried, and activated under vacuum at 120 °C for 1 day. The final product was utilized for the subsequent photocatalytic investigation.

2.5. Photocatalytic mechanism

To elucidate the nature of the Cr(VI) photocatalytic reduction into Cr(III) over HCMUE-2, trapping experiments were conducted to confirm which agents will appear in the reaction solution after photocatalysis. The scavengers, which are utilized to capture the active species, such as electrons, holes, $OH^{\bullet}$, and $O^{2-\bullet}$, were 0.1 M $AgNO_3$, 0.1 M EDTA-2Na, 0.1 M IPA, and 0.1 M *p*-benzoquinone (*p*-BzQ), respectively. Similarly, 15 mg of HCMUE-2 was constantly stirred into an accurate volume of Cr(VI) (10 mg L^{-1}) for 60 min in the dark to reach adsorption–desorption equilibrium before irradiation. Subsequently, the mixture was introduced to each mentioned scavenger and stirred for 90 min at room temperature under visible light from a white LED lamp. Next, 5 mL of the suspension was taken out after each 15 min period, centrifuged, and identified by UV-vis spectroscopy to confirm the remaining concentration of Cr(VI) after the reaction. Based on these surveys, a mechanism for the photocatalytic reduction was proposed along with the difference in photoreduction efficiency in each experiment.

3. Results and discussion

3.1. Complete characterizations of HCMUE-2

To explore the excellent performance for photoreduction of Cr(VI) into Cr(III) over a MOF platform, we assumed several design factors: (i) a suitable pore size, which allows effective diffusion of Cr(VI) into internal pore channels, driving a direct reaction with available active sites; (ii) the necessity for dense electron-rich functional groups to narrow the band gap energy *via* convenient transport from linker to metal-oxo clusters and enhance the adsorption capacity of Cr(VI) in an acidic medium; and (iii) high thermal and water robustness to endure the harsh conditions corresponding to photocatalytic applications. Inspired by this, a mixture of $H_2NDC(OH)$ linker and $ZrOCl_2 \cdot 8H_2O$ was dissolved in DMF solvent in the presence of formic acid as a modulator and heated at 120 °C for 3 days to achieve a brown powder, denoted HCMUE-2 (Fig. 1a). The product was then washed with DMF to remove the unreacted starting chemicals. Subsequently, the solid was exchanged with MeOH and activated under vacuum conditions at 120 °C for 1 day to detach the guest molecules from HCMUE-2. Here, HCMUE-2 possesses a three-dimensional architecture with bcu topology and densely dispersed hydroxyl groups within the structure. This results in a significant improvement in the interaction between the negatively charged Cr(VI) moieties with positively charged OH_2^+ species at low pH values, and supports the electron transfer process from ligand to clusters to form an appropriate band gap energy for the efficient absorption of visible light. The phase purity of as-synthesized HCMUE-2 was determined using powder X-ray diffraction (PXRD) measurement, where the PXRD pattern of the as-synthesized material is in good agreement with the simulated structure. It is realized that the crystallinity of the activated sample was lost under activation, as confirmed by PXRD analysis (Fig. 1b). Additionally, this phenomenon is indicated in the N_2 adsorption isotherm curve and pore size distribution analysis at 77 K of HCMUE-2 (Fig. S4, ESI†). In detail, the BET surface area of HCMUE-2 is much lower than the theoretical specific surface value. This can be explained by the high flexibility of OH moieties inside the backbone upon activation, as illustrated in reported studies.[29–31,46] Interestingly, the level of structural order is entirely recovered upon re-solvation in H_2O (Fig. 1b). The continuous FT-IR spectroscopy analyses of activated HCMUE-2 are revealed in Fig. 1c, compared to the $H_2NDC(OH)$ spectrum. As a result, there are new absorption bands located at 1654, 1601, 1432, and 648 cm^{-1}, which are exhibited in the HCMUE-2 spectrum, but are absent from $H_2NDC(OH)$. These characteristic signals are assigned to the vibrations of uncoordinated C–O in the COOH group, asymmetric C–O, symmetric C–O, and Zr–O within HCMUE-2, respectively. Additionally, the

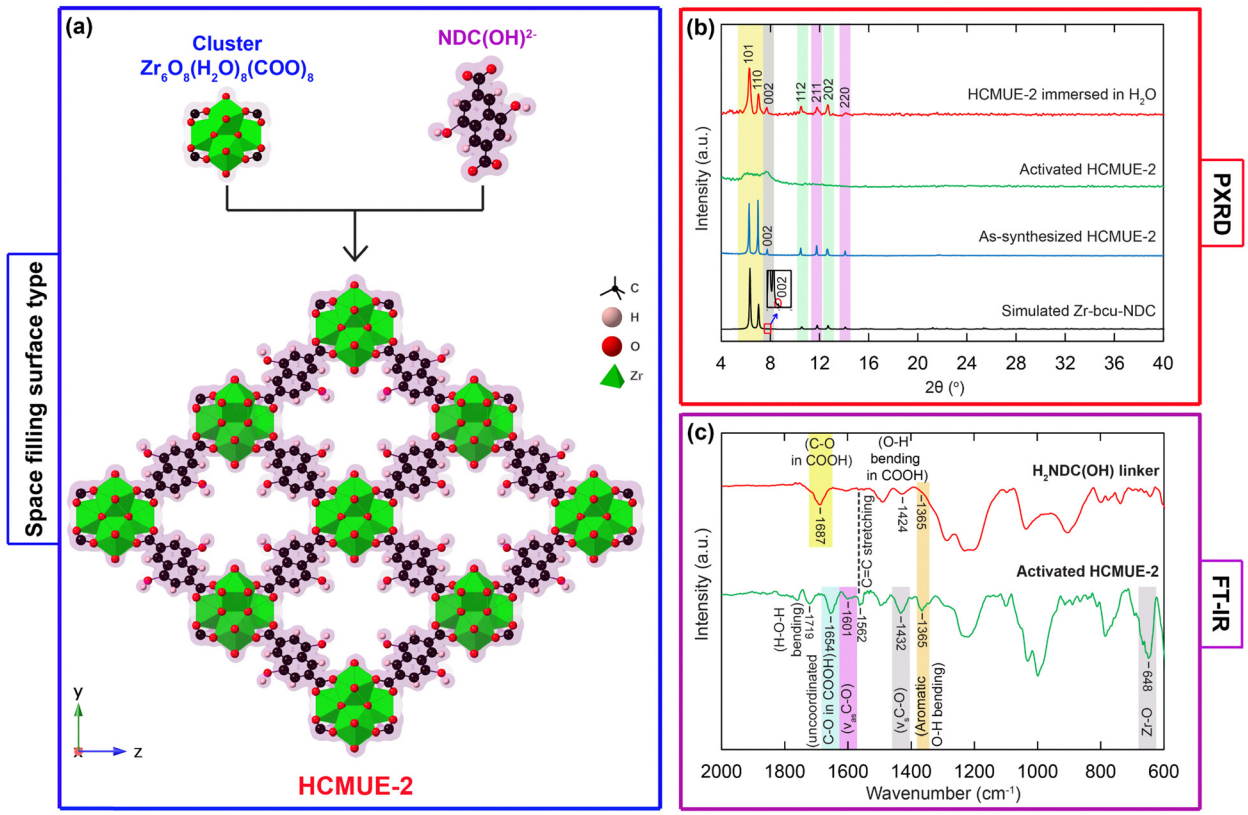

Fig. 1 The structure of HCMUE-2 is formed from $Zr_6O_8(H_2O)_8(COO)_8$ SBUs with $H_2NDC(OH)$ linker (a). Atom colors: Zr, green; C, black; O, red. All H atoms are omitted for clarity. The PXRD patterns of as-synthesized HCMUE-2 (blue), activated HCMUE-2 (green), and HCMUE-2 immersed in H_2O in comparison with simulated Zr-bcu-NDC (b). Fourier transform infrared spectra of $H_2NDC(OH)$ (red) and activated HCMUE-2 (green) (c).

appearance of a vibration mode peaking at 1365 cm^{-1}, is ascribed to the absorption frequency of aromatic O–H bending in both $H_2NDC(OH)$ and HCMUE-2. Additionally, the characteristic mode at 1562 cm^{-1} in both samples is attributed to C=C stretching vibration in the benzene ring derived from the linker. Furthermore, Raman spectra of the HCMUE-2 material and the $H_2NDC(OH)$ linker are shown in Fig. S5 (ESI†). The vibration modes located at the new frequencies, such as 1598 and 1364 cm^{-1}, were relevant to the C=C and C–O bands, respectively, in the spectrum of HCMUE-2, but appeared at various frequency ranges for $H_2NDC(OH)$. In particular, the vibration signal of Zr–O presented at 628 cm^{-1} is also found in HCMUE-2, similar to the stated FT-IR spectrum.

In order to gain a deeper insight into the structural characterizations of HCMUE-2, thermogravimetric analysis combined with differential scanning calorimetry (TGA-DSC), scanning electron microscopy (SEM) incorporating energy-dispersive X-ray (EDX) spectroscopy and mapping, transmission electron microscopy (TEM) analysis, and X-ray photoelectron spectroscopy (XPS) measurement were carried out on the activated HCMUE-2 sample. Consequently, the TGA-DSC curve recorded in a dry air medium are given specifically in Fig. 2a. As a consequence, a weight decrease of 20.46% is attributed to the release of coordinated water inside the clusters of HCMUE-2, and absorbed water on the surface of the material from room temperature to 300 °C, with an initial specific endothermic peak at 107.7 °C. Subsequently, the weight loss of 39.39% in the region from 300 to 600 °C with a strong exothermic peak at 517.9 °C is assigned to the total breakdown of the architecture. Thus, the structural stability of HCMUE-2 is revealed to be thermally stable up to 300 °C. This indicates the promising applications of the HCMUE-2 material in real-life conditions. In addition, the EDX spectrum and EDX-mapping analyses are exhibited in Fig. 2b and Fig. S7 (ESI†), corresponding to the full presence of C, O, and Zr elements within HCMUE-2. The surface morphology of HCMUE-2 is confirmed by SEM and TEM images (Fig. 2c and d), which show that HCMUE-2 possesses prism particles with relative uniformity due to the partial agglomeration with an average size from 50 to 100 nm. Notably, the XPS spectra exhibit the distribution of the C, O, and Zr components within HCMUE-2 (Fig. 3a). Furthermore, the high-resolution XPS spectra were investigated to determine the elemental components on the MOF surface (Fig. 3b–d). Specifically, the C 1s spectrum is deconvoluted into four

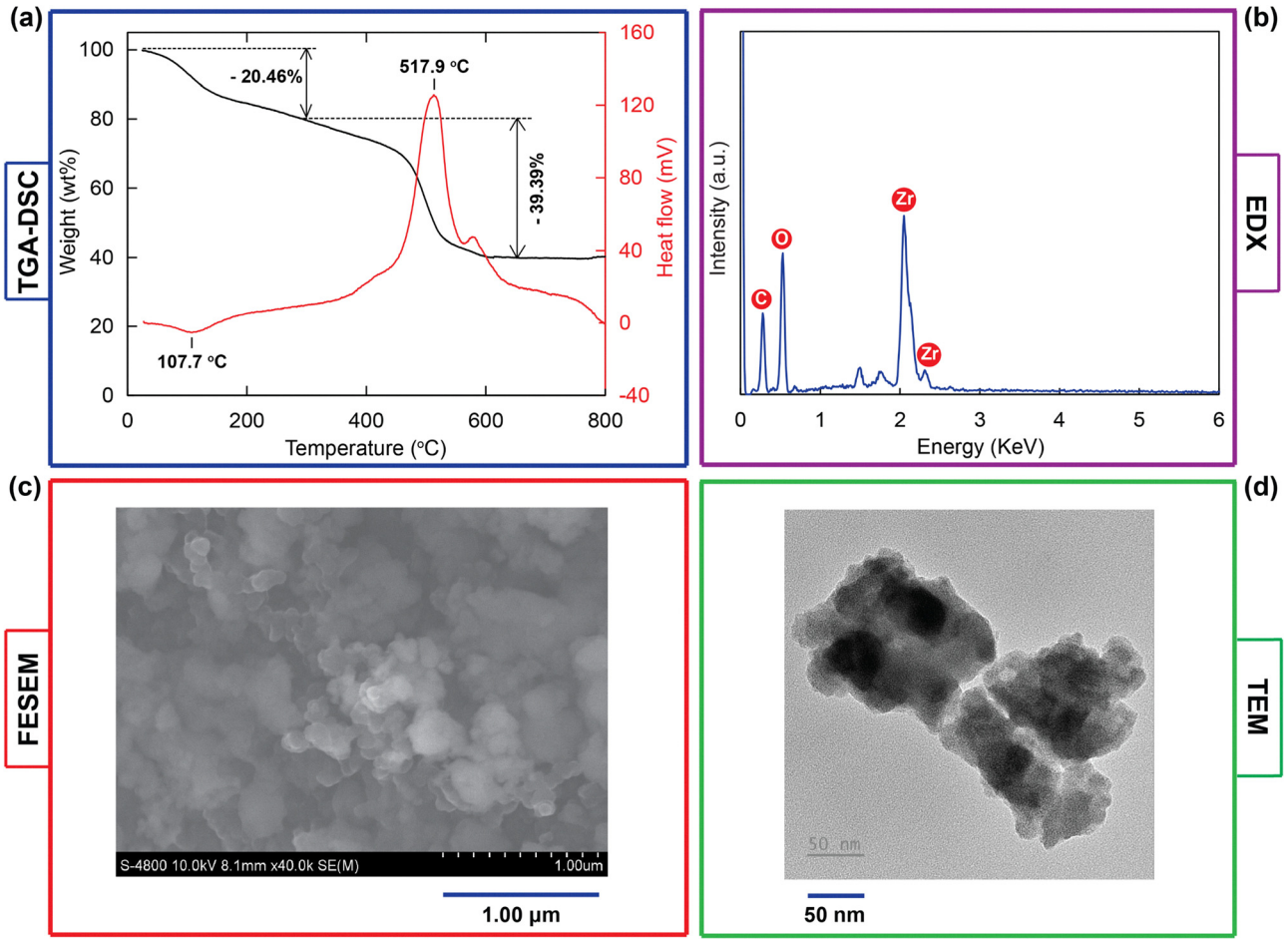

Fig. 2 (a) TGA diagram (black) and DSC curve (red) of activated HCMUE-2; (b) EDX spectrum of activated HCMUE-2; (c) SEM image of activated HCMUE-2 with scale bar of 1.00 µm; (d) TEM image of HCMUE-2 with scale bar of 50 nm.

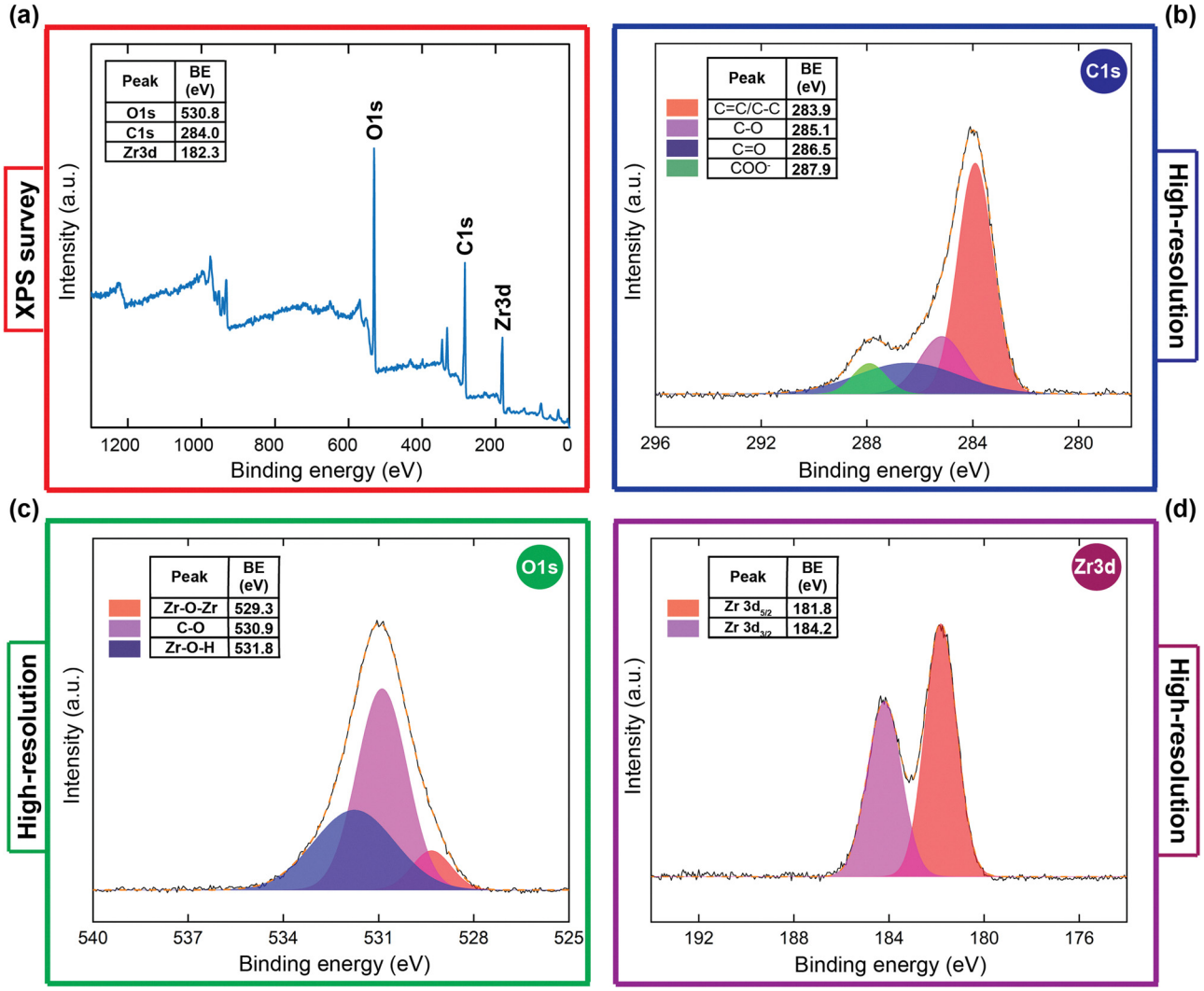

Fig. 3 XPS analysis of HCMUE-2: XPS survey of HCMUE-2 (blue) (a); high-resolution spectrum of C 1s in HCMUE-2 (b); high-resolution spectrum of O 1s in HCMUE-2 (c); high-resolution spectrum of Zr 3d in HCMUE-2 (d).

distinctive peaks at 287.9 eV for the COO^- group, 286.5 eV for the C═O bond, 285.1 eV for the C–O bond, and 283.9 eV for the C═C/C–C bond.[47,48] Next, the high-resolution spectrum of the O 1s curve shows characteristic peaks at 531.8 eV, 530.9 eV, and 529.3 eV, attributed to the appearance of Zr–O–H, C–O, and Zr–O–Zr signals within HCMUE-2.[49,50] Noteworthily, the Zr curve is divided into two peaks at 184.2 eV and 181.8 eV, related to Zr $3d_{3/2}$ and Zr $3d_{5/2}$, respectively.[51] These findings are in good accord with the aforementioned FT-IR and Raman data. This confirmatory evidence proves that the HCMUE-2 material has been successfully fabricated with unique performance that can be utilized for potential applications in practical situations.

3.2. Photoabsorption and electrochemical properties

This fact reveals that the photoabsorption performance of the material plays a vital role in enhancing the photoreduction efficiency of Cr(VI). Hence, UV-vis/DRS analysis was performed on the activated HCMUE-2 sample to explore its behavior. As indicated in Fig. 4a, the HCMUE-2 material exhibits notable photoabsorption with a broad absorption wavelength region from 200 to 1000 nm. This is suitable for the application of HCMUE-2 as an effective photocatalyst in the visible light range. As a result, by fitting the photoabsorption parameters with the indirect transition combined with the Tauc plot (Fig. 4b), the band gap value of HCMUE-2 is 2.12 eV. This obtained result proves that HCMUE-2 displays extraordinary photoabsorption in visible light. This can be accounted for by the highly integrated network between the π electrons in the benzene ring and non-bonding electron pairs of the OH moieties within the HCMUE-2 structure, leading to the formation of a unique chemical optical property.[40] In order to interpret further the stated band gap value of HCMUE-2, electrochemical measurement was conducted. Accordingly, cyclic voltammetry analysis was carried out at a scan rate of 50 mV s^{-1} (Fig. 4c). Here, an inversion layer is created when the applied potential is below the HOMO level; in addition, an accumulation layer is

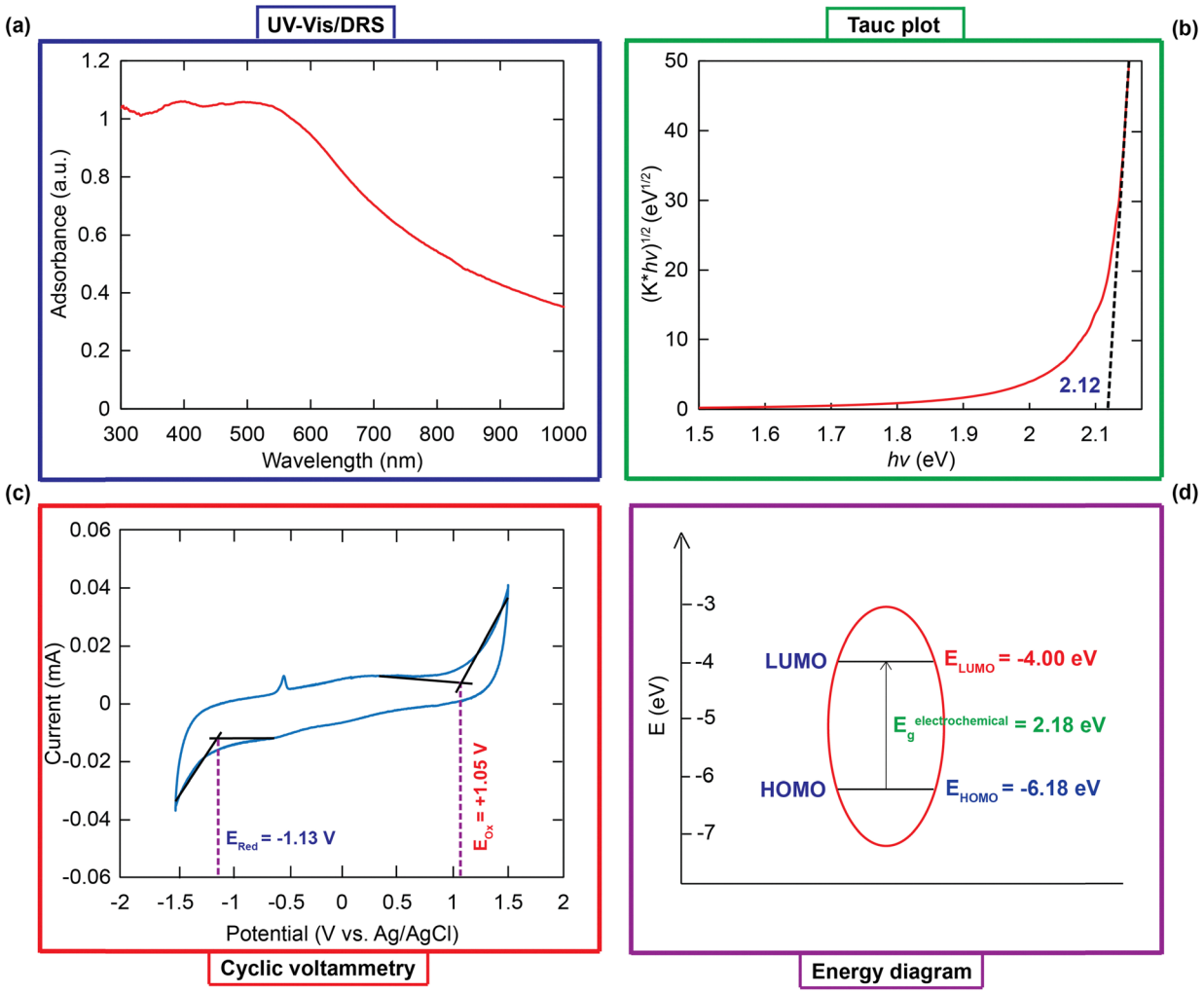

Fig. 4 The UV-vis/DRS spectrum of HCMUE-2 (a); plot of $(K \times h\nu)^{1/2}$ as a function of photon energy for HCMUE-2 (b); the cyclic voltammetry curve of HCMUE-2 (c); the energy diagram of HCMUE-2 indicating the parameters E_{LUMO} and E_{HOMO} (d). The E_{HOMO} and E_{LUMO} values were calculated using the oxidation and reduction signals in combination with electron hole injected into the conduction and valence bands, respectively, following the equations: $E_{HOMO} = -e(E_{ox} + E_{Ref} + 4.50\ V)$ (eV) and $E_{LUMO} = -e(E_{red} + E_{Ref} + 4.50\ V)$ (eV).

formed when the applied potential is above the LUMO level, resulting in the observed change between anodic and cathodic currents (Fig. 4c).[40,52,53] Interestingly, the oxidation and reduction peaks are found at +1.05 V and −1.13 V, allowing determination of the E_{LUMO} and E_{HOMO} values of −4.00 eV and −6.18 eV, respectively. With the achieved results, the value of $E_g^{electrochemical}$ is calculated to be 2.18 eV from the energy diagram (Fig. 4d), corresponding to $E_g^{optical}$ determined from the Tauc plot.

To further elucidate the possible causes behind the enhanced photoreduction of HCMUE-2, the photoluminescence spectrum was recorded from 450 to 700 nm upon an excitation wavelength of 250 nm to confirm the separation efficiency of the electrons and holes for enhancing effective photocatalytic reduction.[54] It has been realized that holes and electrons are key factors during the photocatalytic process because the PL spectrum derives from the recombination of holes and photoinduced electrons. Herein, the low PL signal intensity at the fluorescence peak leads to a low recombination rate between the photogenerated electrons and holes.[55,56] As shown in Fig. 5a, the PL spectrum of HCMUE-2 possesses a relatively small fluorescence intensity at 560 nm, indicating the decrease in the recombination rate of the charge carriers and improvement in photocatalytic efficiency. This can be ascribed to the dense presence of hydroxyl groups within the MOF backbone, facilitating convenient transfer of photoinduced electrons from the ligand to Zr–O clusters and effectively preventing the recombination of holes and electrons. This situation is the same as for the PL spectrum of hydroxyl-functionalized UiO-66.[57] Subsequently, to obtain a deeper comprehension of photo-excited carrier transport, the time-resolved fluorescence decay spectrum of HCMUE-2 was performed (Fig. 5b). As a result, the HCMUE-2 sample exhibits an exponential decline in fluorescence intensity with sluggish kinetics. Through fitting of the decay spectrum, the lifetime of HCMUE-2 is calculated to be 34.51 ns. This value points out

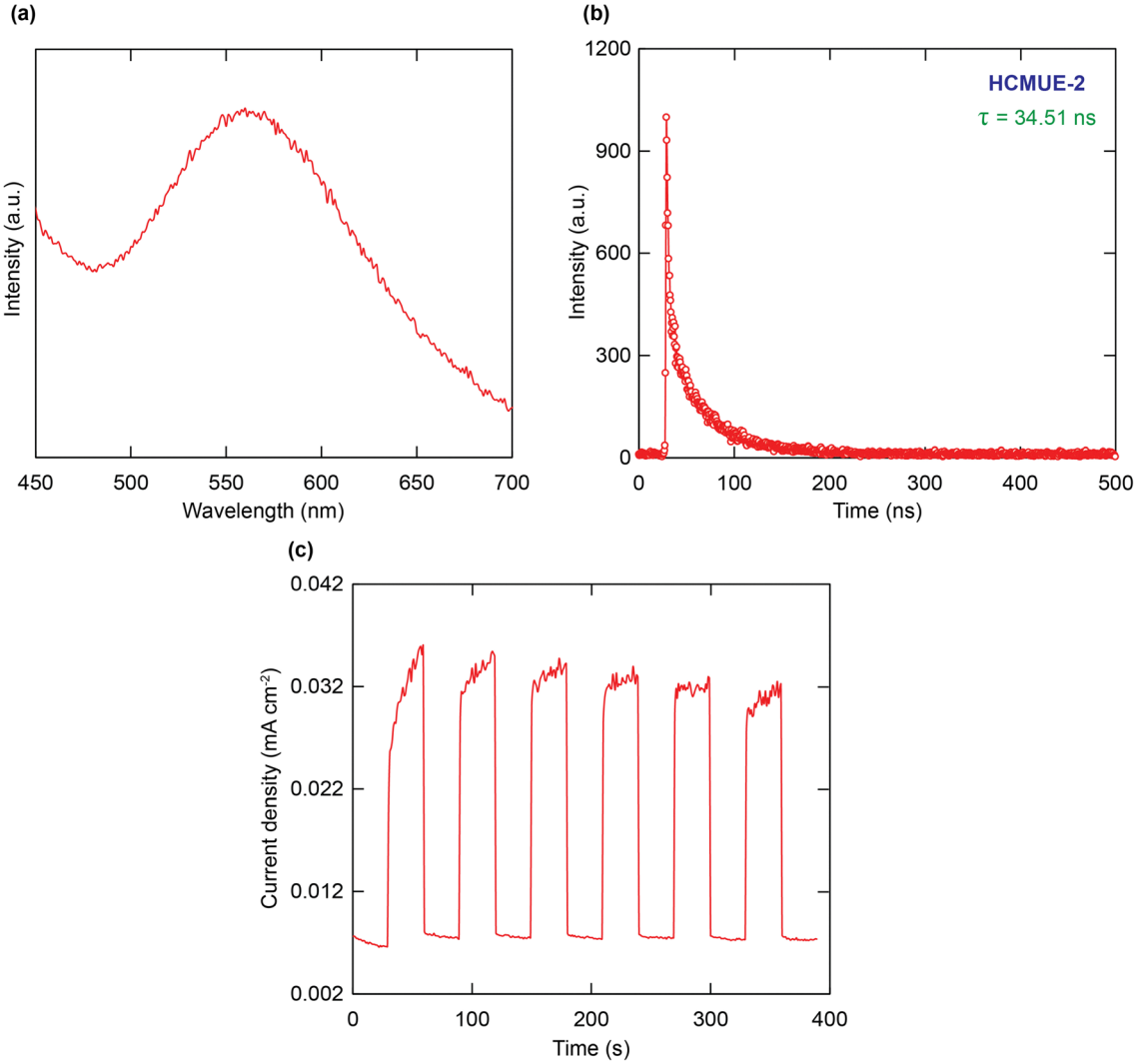

Fig. 5 The PL spectrum of HCMUE-2 with an excitation wavelength of 250 nm (a); time-resolved transient photoluminescence decay spectrum of HCMUE-2 (b); transient photocurrent response of HCMUE-2 (c).

the considerable protraction of the lifetime of the photogenerated electrons and holes, resulting in boosting their separation efficiency in the photocatalytic process and inhibiting their recombination. It is interesting to note that the enhanced lifetime of the electrons and holes depends on the optimal electron transfer and the band structure change caused by the efficient functionalization of OH moieties onto the MOF architecture, driving the formation of huge π–π and π–p integrated electron systems derived from the unpaired electrons of hydroxyl groups in the linkers and clusters, and π-electron networks of benzene rings.[58] Moreover, the photocurrent–time diagram of HCMUE-2 for six on–off cycles with discrete visible light illumination is clearly displayed in Fig. 5c. It is found that the current density rises upon visible light irradiation, which is attributed to the increase in separation level of photo-excited carriers. Whereas, the photocurrent density decreases to zero without light illumination. This finding can be explained by the effective transport of photoinduced electrons from the linker to the catalytic sites of the Zr–O clusters.[59]

3.3. Photoreduction of Cr(VI)

To explore the excellent photocatalytic reduction of Cr(VI) over HCMUE-2 caused by the dense packaged presence of the OH moieties within the architecture, a series of photoreduction studies were conducted. In detail, the HCMUE-2 material (15 mg) was introduced to 40 mL of Cr(VI) solution at a concentration of 10 mg L^{-1} in an initial pH region from 1 to 5. The mixture was stirred at a constant rate for 60 min in the dark to achieve adsorption–desorption equilibrium before visible light illumination. As shown in Fig. 6a, no considerable conversion of Cr(VI) into Cr(III) is observed in the absence of a photocatalyst under visible light in 90 min. While, in the dark, HCMUE-2 reveals the uptake of Cr(VI) at about 43% at pH = 1, attributed to the pure adsorption of Cr(VI) into the internal pore channels of the MOF structure (Fig. 6a and b). Herein, the uptake process of

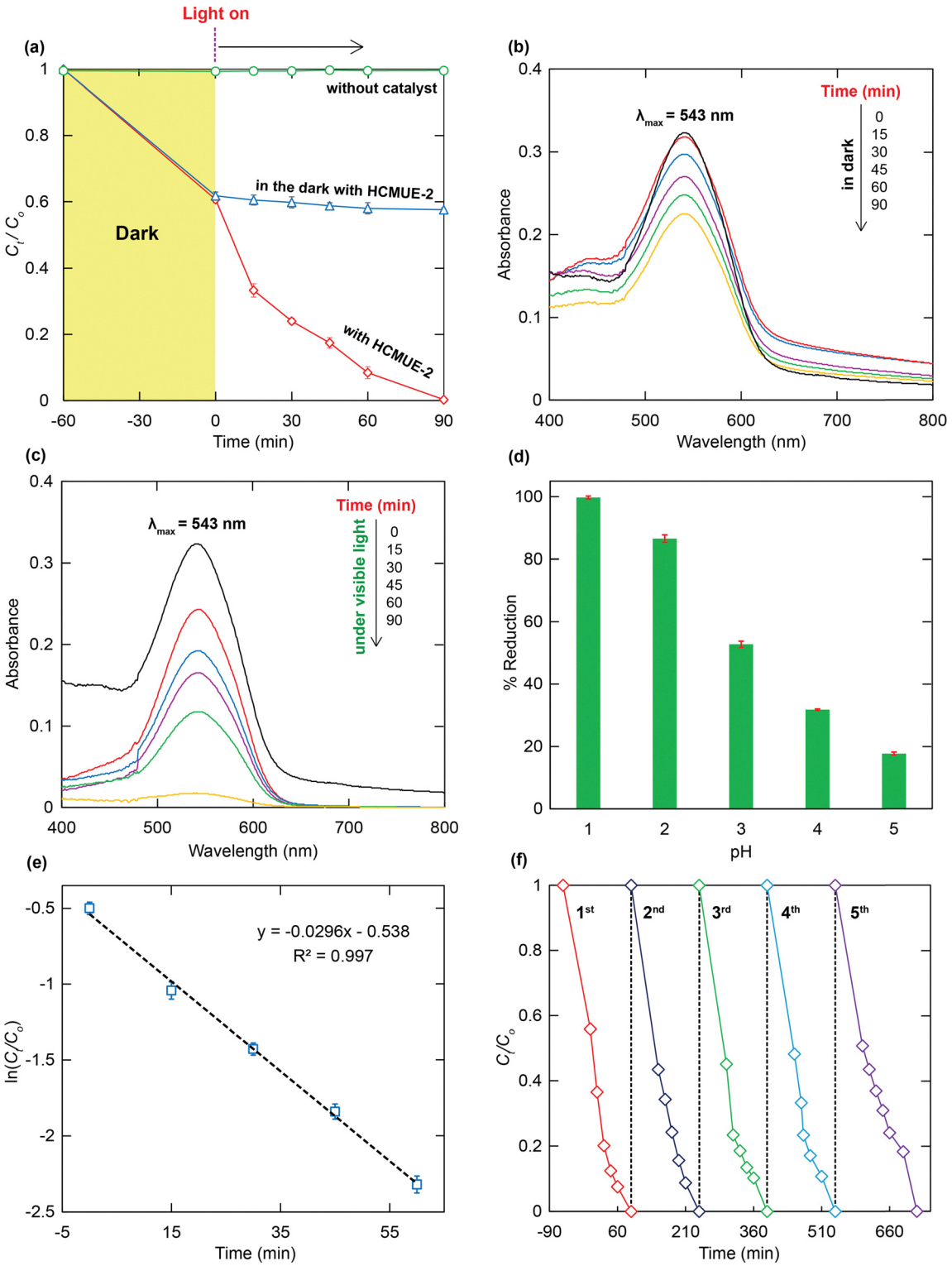

Fig. 6 The Cr(VI) photoreduction reaction under visible light and in the dark by HCMUE-2, and without the photocatalyst under visible light (a); UV-vis absorption spectra of Cr(VI) over HCMUE-2 with different intervals in the dark (b), and under visible light (c); the photoreduction percentage of Cr(VI) in media of different pH (d); plot of $\ln(C_t/C_0)$ *versus* time for Cr(VI) photoreduction over HCMUE-2 (e); photocatalytic profile of Cr(VI) by HCMUE-2 over five consecutive cycles (f).

Cr(VI) into the pore channel of HCMUE-2 in a low-pH medium is supported by the protonation of hydroxyl groups inside the structure, driving the formation of OH_2^+ species capable of effective interaction with the negatively charged Cr(VI) ions from solution. Furthermore, as in our previous report,[46] the point of zero charge (pH_{pzc}) of HCMUE-2 was determined to be

Table 1 The maximum photoreduction of Cr(VI) by HCMUE-2 in comparison with the other photocatalysts

Material	Dosage (g L^{-1})	C_0 (mg L^{-1})	Efficiency (%)	Time (min)	Ref.
$SrTiO_3$	1.0	4.8	99	240	60
OH-TiO_2	1.0	10	88	30	61
Ag-BiOCl	1.0	10	86	180	62
MIL-53(Fe)	1.0	20	66	40	63
Ag/AgCl@MIL-53(Fe)	0.4	10	99.4	240	64
g-C_3N_4/UiO-66	0.5	10	99	40	65
UiO-66-NH_2(Zr)	0.5	5	98	120	66
MIL-53-NH_2	0.5	8	15	60	67
RGO-UiO-66(NH_2)	0.5	10	100	100	68
MIL-100/$Bi_{12}O_{17}C_{12}$	0.5	10	99.2	120	69
MIL-101-NH_2/g-C_3N_4	1.0	20	66	90	70
MIL-53/WO_3	1.0	45	94	240	71
HCMUE-2	**0.375**	**10**	**93**	**60**	**This**
	0.375	**10**	**100**	**90**	**study**

4.2, leading to efficient enhancement of the possible uptake of Cr(VI) *via* the electrostatic attraction between the positive surface charge and Cr(VI) anions at pH values lower than pH_{pzc}. Notably, HCMUE-2 has an extraordinary photocatalytic reduction performance for Cr(VI), reaching an efficiency of 100% upon irradiation by visible light in 90 min at pH = 1 (Fig. 6a and c). This unique efficiency can be ascribed to the efficient support of the hydroxyl groups inside HCMUE-2, which helps enhance the convenient non-bonding electron transfer to the π–π integration system in the architecture of the material and improving the photoabsorption property under visible light by decreasing the band gap value.[40] The obtained result in the photoreduction of Cr(VI) into Cr(III) over HCMUE-2 is significantly greater than those for published investigations in terms of the simpler and milder experimental conditions in respect of the MOF dosage and initial Cr(VI) content (Table 1). This fact shows that the OH moieties present in the linkers and clusters will promote the removal of Cr(VI) *via* the adsorption mechanism by the protonation reaction under acidic pH conditions, leading to the generation of $-OH_2^+$ species and effectively interacting electrostatically with the anionic Cr(VI) species. Accordingly, there is complete photoreduction efficiency for Cr(VI), which is found at pH = 1 under

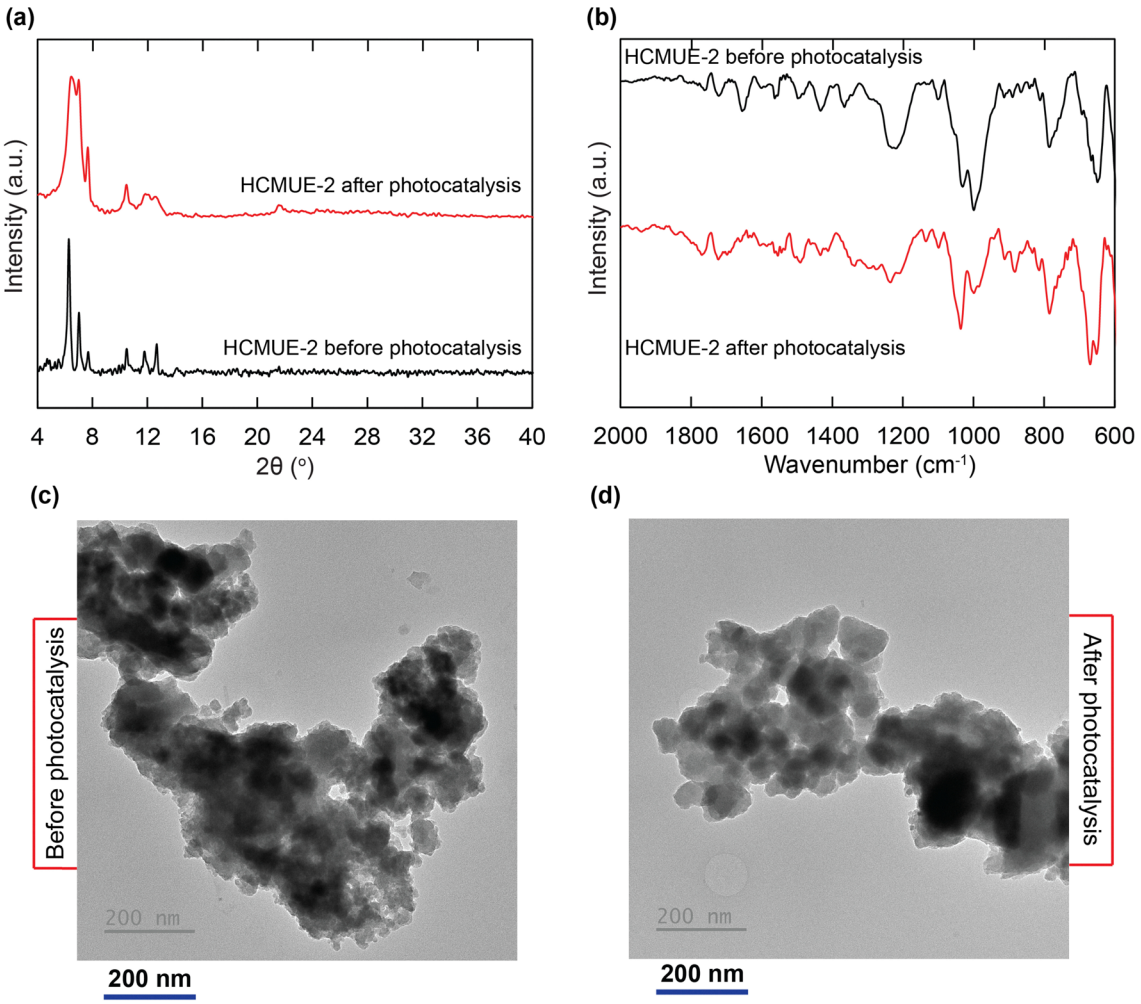

Fig. 7 The PXRD diagram of HCMUE-2 before photoreduction of Cr(VI) (black) compared to the PXRD pattern of HCMUE-2 after photoreduction (red) (a); FT-IR spectrum of HCMUE-2 before photocatalysis of Cr(VI) (black) and after photocatalysis of Cr(VI) (red) (b); TEM images of HCMUE-2 before photoreduction of Cr(VI) (c) and after reusability (d) with a scale bar of 200 nm.

visible light irradiation after 90 min for HCMUE-2. Whereas, the photocatalytic reduction yield for Cr(VI) gradually rises to 18% for pH = 5, 32% for pH = 4, 53% for pH = 3, and 86% for pH = 2, in 90 min (Fig. 6d). A series of investigations of the photoreduction of Cr(VI) over HCMUE-2 in neutral and basic media was also conducted to evaluate the wider applicability of the material, exhibiting poor photocatalytic possibilities for HCMUE-2 under these conditions (Fig. S11, ESI†). Herein, the lower Cr(VI) photoreduction percentage at pH over 1 can be explained by the creation of different Cr(VI) species and the precipitation of chromium(III) hydroxide, resulting in their occupation of the pore cavities of the MOF causing obstacles to active adsorption and photoreduction sites within HCMUE-2.[40,72]

Photoreduction kinetics were also studied to gain an insight into the photocatalytic behavior of HCMUE-2. Consequently, the kinetic parameter is best fitted with the pseudo-first-order model (Section S8, ESI†), indicating a high correlation coefficient of 0.997 (Fig. 6e). Furthermore, the rate constant parameter of the Cr(VI) photoreduction process over HCMUE-2 reached a value of 0.0296 min^{-1} at pH = 1, which is higher than those of other reported photocatalysts. In particular, the regeneration possibility of the material after the photoreduction was surveyed to demonstrate its use efficiency in practical situations. HCMUE-2 was collected, immersed in 1% nitric acid solution to totally dissolve the $Cr(OH)_3$ species remaining in the pores and washed with an excess amount of H_2O until pH = 7. Next, the product was exchanged in MeOH, centrifuged, and activated under vacuum for 24 h at 120 °C for subsequent reusability studies. As illustrated in Fig. 6f, the photoreduction ability for Cr(VI) by HCMUE-2 is retained over five consecutive cycles at pH = 1 after 120 min of irradiation with visible light with an inconsiderable decline.

Additionally, the architectural robustness of HCMUE-2 after five cycles was determined by additional analyses, including PXRD, FT-IR, Raman, and TEM. As a consequence, the structural order of the material is retained, as evidenced by the PXRD patterns of HCMUE-2 before and after the photocatalytic reaction, in good agreement with the diffraction peaks (Fig. 7a). Moreover, the characteristic bands of vibrational modes observed from the FT-IR and Raman spectra, within HCMUE-2 after photoreduction are in good accord with the pristine sample (Fig. 7b and Fig. S6, ESI†). Noteworthily, there is no significant difference in the surface morphology of the material in terms of particle size after five recycles (Fig. 7c, d and Fig. S8, ESI†). These observations demonstrated that HCMUE-2 could be utilized as a promising material in the photocatalytic reduction of Cr(VI) into Cr(III) from wastewater.

3.4. Proposed photoreduction mechanism of Cr(VI)

To further understand the Cr(VI) photoreduction process over a hydroxyl-modified Zr-based MOF, a series of experiments were

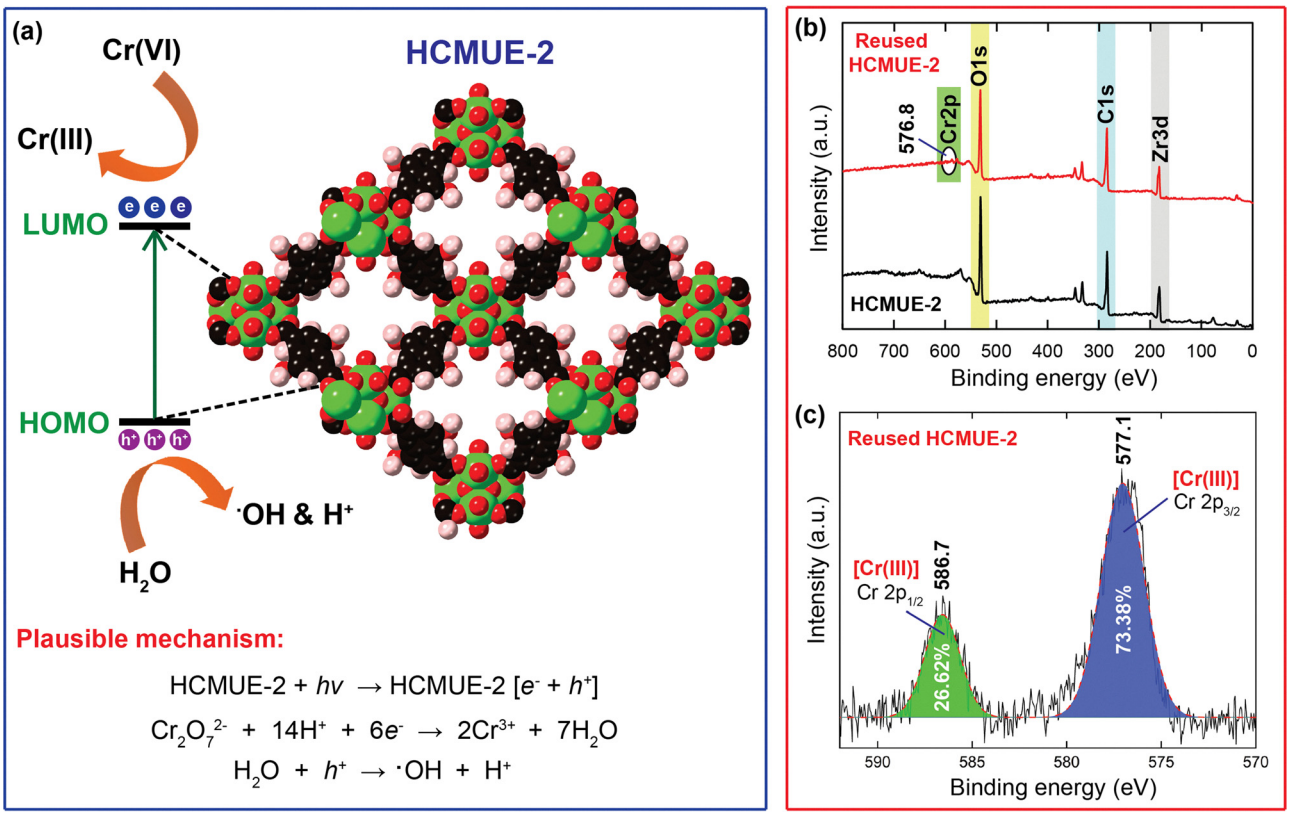

Fig. 8 Possible photoreduction mechanism of Cr(VI) over HCMUE-2 (a); XPS measurements of HCMUE-2: the XPS survey of sample before photocatalysis (black), and after photocatalysis (red) (b); the Cr 2p high-resolution XPS spectrum of recycled HCMUE-2 after the Cr(VI) photoreduction study under visible light (c).

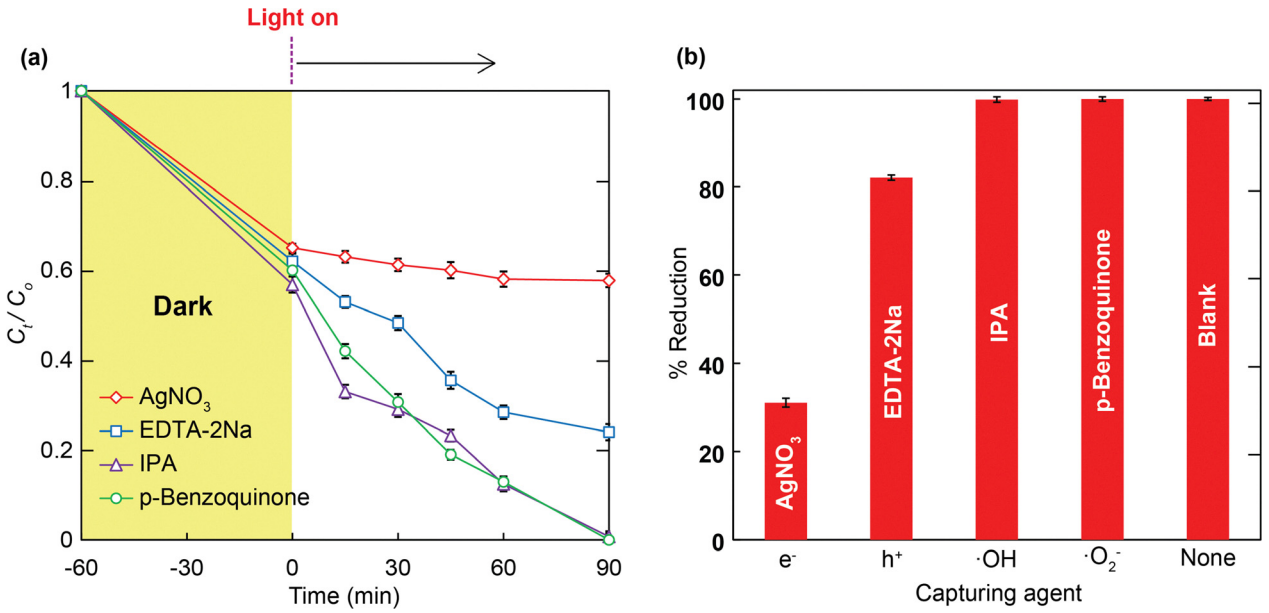

Fig. 9 The Cr(VI) photoreduction reaction under visible light over HCMUE-2 in the presence of scavengers (a); influence of various scavengers on Cr(VI) photoreduction efficiency over HCMUE-2 (b).

conducted to explore the photoreduction mechanism. As revealed in Fig. 8a, before exposure to light, the anionic Cr(VI) species that existed at a low-pH range moved to the external and internal pores of HCMUE-2 *via* the efficient electrostatic attraction generated by the anionic Cr(VI) species and protonated hydroxyl groups within the MOF backbone. The photocatalyst gains continuous exposure to visible light owing to higher or the same energy as the band gap energy of the material, causing an excitation of electrons (e^-) from the valence to the conduction zone and the generation of holes (h^+). Notably, the elementary photogenerated electrons, created by the OH groups inside the structure, will be transferred to the metal clusters through ligand-to-metal oxo charge carrier transport. These electrons rapidly go to the HCMUE-2 surface, where they will combine with the protons to reduce the Cr(VI) species to Cr(III). Simultaneously, the water molecules, as hole scavengers, incorporate the holes to create protons and $^{\bullet}OH$ radicals.[40,73] To demonstrate the appearance of Cr(III) ions during the photoreduction process, HCMUE-2 was collected by centrifugation prior to XPS measurement. Accordingly, the new signal peak appears at 576.8 eV, which is assigned to the binding energy of Cr 2p within the reused sample (Fig. 8b). In particular, the high-resolution curve of Cr 2p of the recycled HCMUE-2 indicates the appearance of the Cr(III) species with the characteristic peaks at 586.7 eV for Cr $2p_{1/2}$ and 577.1 eV for Cr $2p_{3/2}$,[74,75] and the absence of Cr(VI) ions inside the architecture, proving the complete reduction of Cr(VI) into Cr(III) (Fig. 8c). The obtained data illustrate that Cr(III) is formed and almost absorbed into the pore channel of HCMUE-2 after the Cr(VI) photoreduction reaction. To elucidate the stated argument, the solution extract after 90 min of photocatalysis was analyzed by atomic absorption spectroscopy (AAS) to determine the total remaining Cr content after the reaction. The results showed that the remaining Cr content in the solution present after the reaction reached the permitted concentration.

To further demonstrate the abovementioned photocatalytic mechanism, various scavengers, including $AgNO_3$, EDTA-2Na, isopropanol (IPA), and *p*-benzoquinone, were added to the photocatalytic reaction system to trap e^-, h^+, $^{\bullet}OH$, and $^{\bullet}O_2^-$, respectively,[24,76] and the results are clearly exhibited in Fig. 9. As a result, the Cr(VI) photoreduction efficiency reaches almost 100% compared to the blank sample after the introduction of IPA and *p*-benzoquinone scavengers. This proves that the trapping agents for $^{\bullet}OH$ and $^{\bullet}O_2^-$ show no activity throughout the photocatalytic reaction. However, the photocatalytic reduction percentage of Cr(VI) declines considerably to 82% and 31% as the scavengers for EDTA-2Na and $AgNO_3$ are added to the reaction mixture, respectively, indicating that both active moieties, h^+, and e^-, directly join the photoreduction reaction, especially e^-.

4. Conclusion

We have described the synthesis and full characterization of a Zr-based MOF with modification by hydroxyl groups, namely HCMUE-2. The HCMUE-2 material displayed an extraordinary photoreduction performance for Cr(VI) under visible light illumination. Accordingly, the great Cr(VI) photocatalytic reduction yield over HCMUE-2 reached 100% after 90 min at pH = 1 upon irradiation by visible light, with the reduction efficiency being maintained without any significant loss for at least five consecutive cycles. To the best of our knowledge, this obtained yield is much higher than that of previously reported studies in terms of the treated initial concentration of Cr(VI) and the dosage of photocatalyst. Significantly, the architectural stability of HCMUE-2 after the photoreduction reaction is confirmed by

the incorporated PXRD, FT-IR, Raman spectra, and TEM measurements. Moreover, the possible Cr(VI) photoreduction mechanism and formed Cr(III) species are interpreted *via* trapping experiments for the reaction agents combined with the XPS spectrum. Additionally, the cost-effectiveness of using HCMUE-2 under practical conditions is reasonable, with its facile large-scale synthesis, small amounts of photocatalyst in the photoreduction process, and high reusability. The results achieved in this work promise the opening up of photocatalytic fields of OH-functionalized Zr-based MOFs and will boost novel research for modified materials in treating the highly poisonous Cr(VI) ions from wastewater.

Author contributions

M. V. N. formulated this project. M. V. N., V. T. L., and A. T. D. P. prepared the linker and material and collected the PXRD patterns, FT-IR, Raman spectra, TGA-DSC, and UV-vis measurements. M. V. N. wrote the paper, and all authors contributed to revising it. All authors have given approval to the final version of the manuscript.

Conflicts of interest

The authors maintain that they have no conflict of interest for this communication.

Data availability

Data available on request from the corresponding author.

Notes and references

1 P. Grennfelt, A. Engleryd, M. Forsius, O. Hov, H. Rodhe and E. Cowling, Acid rain and air pollution: 50 years of progress in environmental science and policy, *Ambio*, 2020, **49**, 849–864.
2 E. Wołejko, A. Jabłońska-Trypuć, U. Wydro, A. Butarewicz and B. Łozowicka, Soil biological activity as an indicator of soil pollution with pesticides – A review, *Appl. Soil Ecol.*, 2020, **147**, 103356.
3 K. Shekhawat, S. Chatterjee and B. Joshi, Chromium toxicity and its health hazards, *Int. J. Adv. Res.*, 2015, **3**, 167–172.
4 C. C. Alvarez, M. E. B. Gómez and A. H. Zavala, Hexavalent chromium: Regulation and health effects, *J. Trace Elem. Med. Biol.*, 2021, **65**, 126729.
5 M. Costa and C. B. Klein, Toxicity and carcinogenicity of chromium compounds in humans, *Crit. Rev. Toxicol.*, 2006, **36**, 155–163.
6 S. Lewicki, R. Zdanowski, M. Krzyzowska, A. Lewicka, B. Debski, M. Niemcewicz and M. Goniewicz, The role of Chromium III in the organism and its possible use in diabetes and obesity treatment, *Ann. Agric. Environ. Med.*, 2014, **21**, 331–335.
7 A. Maleki, B. Hayati, M. Naghizadeh and S. W. Joo, Adsorption of hexavalent chromium by metal organic frameworks from aqueous solution, *J. Ind. Eng. Chem.*, 2015, **28**, 211–216.
8 A. Pholosi, E. B. Naidoo and A. E. Ofomaja, Batch and continuous flow studies of Cr(VI) adsorption from synthetic and real wastewater by magnetic pine cone composite, *Chem. Eng. Res. Des.*, 2020, **153**, 806–818.
9 W. S. W. Ho and T. K. Poddar, New membrane technology for removal and recovery of chromium from waste waters, *Environ. Prog.*, 2001, **20**, 44–52.
10 S. Habibi, A. Nematollahzadeh and S. A. Mousavi, Nanoscale modification of polysulfone membrane matrix and the surface for the separation of chromium ions from water, *J. Chem. Eng.*, 2015, **267**, 306316.
11 Y. Zhao, D. Kang, Z. Chen, J. Zhan and X. Wu, Removal of chromium using electrochemical approaches: A review, *Int. J. Electrochem. Sci.*, 2018, **13**, 1250–1259.
12 N. Hilali, H. Mohammadi, A. Amine, N. Zine and A. Errachid, Recent advances in electrochemical monitoring of chromium, *Sensors*, 2020, **20**, 5153.
13 O. N. Kononova, G. L. Bryuzgina, O. V. Apchitaeva and Y. S. Kononov, Ion exchange recovery of chromium(VI) and manganese(II) from aqueous solutions, *Arabian J. Chem.*, 2015, **12**, 2713–2720.
14 M. Arumugam, Y. Yu, H. J. Jung, S. Yeon, H. Lee, J. Theerthagiri, S. J. Lee and M. Y. Choi, Solvent-mediated synthesis of BiOI with a tunable surface structure for effective visible light active photocatalytic removal of Cr(VI) from wastewater, *Environ. Res.*, 2021, **197**, 111080.
15 C. Li, Z. Zhao, S. Fu, X. Wang, Y. Ma and S. Dong, Polyvinylpyrrolidone in the one-step synthesis of carbon quantum dots anchored hollow microsphere Bi_2WO_6 enhances the simultaneous photocatalytic removal of tetracycline and Cr(VI), *Sep. Purif. Technol.*, 2021, **270**, 118844.
16 S. Rengaraj, S. Venkataraj, J. Yeon, Y. Kim, X. Z. Li and G. K. H. Pang, Preparation, characterization and application of Nd-TiO_2 photocatalyst for the reduction of Cr(VI) under UV light illumination, *Appl. Catal., B*, 2007, **77**, 157–165.
17 L. Yang, Y. Xiao, S. Liu, Y. Li, Q. Cai, S. Luo and G. Zeng, Photocatalytic reduction of Cr(VI) on WO_3 doped long TiO_2 nanotube arrays in the presence of citric acid, *Appl. Catal., B*, 2010, **94**, 142–149.
18 R. Acharya, B. Naik and K. Parida, Cr(VI) remediation from aqueous environment through modified-TiO_2-mediated photocatalytic reduction, *Beilstein J. Nanotechnol.*, 2018, **9**, 1448–1470.
19 Y. Zhao, D. Zhao, C. Chen and X. Wang, Enhanced photoreduction and removal of Cr(VI) on reduced graphene oxide decorated with TiO_2 nanoparticles, *J. Colloid Sci.*, 2013, **405**, 211–217.
20 Y. Yu, K. Wu, W. Xu, D. Chen, J. Fang, X. Zhu, J. Sun, Y. Liang, X. Hu, R. Li and Z. Fang, Adsorption-photocatalysis synergistic removal of contaminants under antibiotic and Cr(VI) coexistence environment using non-metal g-C_3N_4 based nanomaterial obtained by supramolecular self-assembly method, *J. Hazard. Mater.*, 2021, **404**, 124171.

21 M. M. Thwala and L. N. Dlamini, Photocatalytic reduction of Cr(VI) using Mg-doped WO_3 nanoparticles, *Environ. Technol.*, 2020, **41**, 2277–2292.
22 A. Hsini, Y. Naciri, M. Laabd, A. Bouziani, J. A. Navío, F. Puga, R. Boukherroub, R. Lakhmiri and A. Albourine, Development of a novel PANI@WO_3 hybrid composite and its application as a promising adsorbent for Cr(VI) ions removal, *J. Environ. Chem. Eng.*, 2021, **9**, 105885.
23 M. Naimi-Joubani, M. Shirzad-Siboni, J.-K. Yang, M. Gholami and M. Farzadkia, Photocatalytic reduction of hexavalent chromium with illuminated ZnO/TiO_2 composite, *J. Ind. Eng. Chem.*, 2014, **22**, 317–323.
24 H. Zhang, J. Nan, X. Ning, L. Hu, Q. Shao, J. Zhang and Z. Guo, Metal-organic Framework-derived NiO/ZnO composites for photoelectrocatalytic reduction of Cr(VI), *ChemPhotoChem*, 2025, **9**, e202400091.
25 Z. Wu, X. Liu, C. Yu, F. Li, W. Zhou and L. Wei, Construct interesting CuS/TiO_2 architectures for effective removal of Cr(VI) in simulated wastewater via the strong synergistic adsorption and photocatalytic process, *Sci. Total Environ.*, 2021, **796**, 148941.
26 S. M. Majhi, A. Ali, P. Rai, Y. E. Greish, A. Alzamly, S. G. Surya, N. Qamhieha and S. T. Mahmoud, Metal-organic frameworks for advanced transducer based gas sensors: review and perspectives, *Nanoscale Adv.*, 2022, **4**, 697.
27 M. V. Nguyen, T. U. Kim, L. H. T. Nguyen, A. Mirzaei, A. T. T. Pham, T. Q. Tran, N. X. D. Mai, N. Q. Tran, Y. Kim, T. B. Phan, H. W. Kim, S. S. Kim and T. L. H. Doan, Efficient low-temperature detection of CO gas by various metalated porphyrinic-Al-based MOF (Cu and Co) materials, *Sens. Actuators, B*, 2025, **424**, 136915.
28 T. Ghanbari, F. Abnisa and W. M. A. W. Daud, A review on production of metal organic frameworks (MOF) for CO_2 adsorption, *Sci. Total Environ.*, 2020, **707**, 135090.
29 T. T. M. Bui, L. T. Nguyen, N. P. H. Pham, C. C. Tran, L. T. Nguyen, T. A. Nguyen, H. N. Nguyen and M. V. Nguyen, A new approach for ultra-high adsorption of cationic methylene blue in a Zr-sulfonic-based metal-organic framework, *RSC Adv.*, 2021, **11**, 36626–36635.
30 K. M. V. Nguyen, A. V. N. Phan, N. T. Dang, T. Q. Tran, H. K. Duong, H. N. Nguyen and M. V. Nguyen, Efficiently improving the adsorption capacity of the Rhodamine B dye in a SO_3H-functionalized chromium-based metal-organic framework, *Mater. Adv.*, 2023, **4**, 2636–2647.
31 C. C. Tran, H. C. Dong, V. T. N. Truong, T. T. M. Bui, H. N. Nguyen, T. A. T. Nguyen, N. N. Dang and M. V. Nguyen, Enhancing the remarkable adsorption of Pb^{2+} in a series of sulfonic-functionalized Zr-based MOFs: a combined theoretical and experimental study for elucidating the adsorption mechanism, *Dalton Trans.*, 2022, **51**, 7503–7516.
32 Y. Chen, Y. Zhang, Q. Huang, X. Lin, A. Zeb, Y. Wu, Z. Xu and X. Xu, Recent advances in Cu-based metal-organic frameworks and their derivatives for battery applications, *ACS Appl. Energy Mater.*, 2022, **5**, 7842–7873.
33 M. V. Nguyen, T. B. Phan, M. V. Tran, T. A. T. Nguyen and H. N. Nguyen, A confinement of N-heterocyclic molecules in a metal-organic framework for enhancing significant proton conductivity, *RSC Adv.*, 2022, **12**, 355–364.
34 D. T. Nguyen, H. N. Nguyen, T. M. Nguyen, H. C. Dong, N. N. Dang, Q.-H. Tran, T. A. Nguyen, M. V. Tran, T. L. H. Doan, L. C. Luu and M. V. Nguyen, An excellent photodegradation efficiency of methylene blue and rhodamine B dyes in a series of porphyrinic Aluminum-based MOFs metallated by copper and cobalt metals, *Colloids Surf., A*, 2024, **689**, 133663.
35 M. V. Nguyen, H. C. Dong, V. T. N. Truong, H. N. Nguyen, L. C. Luu, N. N. Dang and T. A. T. Nguyen, A new porphyrinic vanadium-based MOF constructed from infinite V(OH)O4 chains: syntheses, characterization and photoabsorption properties, *New J. Chem.*, 2022, **46**, 632–641.
36 Q. Shang, N. Liu, D. You, Q. Chen, G. Liao and Z. Pan, The application of Ni and Cu-MOFs as highly efficient catalysts for visible light-driven tetracycline degradation and hydrogen production, *J. Mater. Chem. C*, 2021, **9**, 238–248.
37 K. Manna, R. Kumar, A. Sundaresan and S. Natarajan, Fixing CO_2 under atmospheric conditions and dual functional heterogeneous catalysis employing Cu MOFs: Polymorphism, single-crystal-to-single-crystal (SCSC) transformation and magnetic studies, *Inorg. Chem.*, 2023, **62**, 13738–13756.
38 H. Kaur, S. Sinha, V. Krishnan and R. R. Koner, Photocatalytic reduction and recognition of Cr(VI): New Zn(II)-based metal-organic framework as catalytic surface, *Ind. Eng. Chem. Res.*, 2020, **59**, 8538–8550.
39 G. Niu, C. Si, J. Jiao, Q. Han, M. Guo and M. Li, An electron-rich metal-organic framework for highly efficient photocatalytic reduction of Cr(VI), *J. Alloys Compd.*, 2020, **830**, 154696.
40 D. T. Nguyen, K. M. V. Nguyen, H. K. Duong, B. T. Nguyen, M. D. K. Nguyen, D. B. Tran, Q.-H. Tran, T. L. H. Doan and M. V. Nguyen, Enhanced photoreduction efficiency of Cr(VI) driven by visible light in a new Zr-based metal-organic framework modified by hydroxyl groups, *Dalton Trans.*, 2024, **53**, 7213–7228.
41 M. Deng, J. Sun, J. Chakraborty, M. Zhou and P. V. D. Voort, From design to applications: A comprehensive review on porous frameworks for photocatalytic volatile organic compounds (VOCs) removal, *ChemCatChem*, 2024, **16**, e202300783.
42 H. Xie, D. Ma, W. Liu, Q. Chen, Y. Zhang, J. Huang, H. Zhang, Z. Jin, T. Luo and F. Peng, Zr-based MOFs as a new photocatalysts for rapid reduction of Cr(VI) in water, *New J. Chem.*, 2020, **44**, 7218–7225.
43 X.-D. Du, X.-H. Yi, P. Wang, W. Zheng, J. Deng and C.-C. Wang, Robust photocatalytic reduction of Cr(VI) on UiO-66-NH_2(Zr/Hf) metal-organic framework membrane under sunlight irradiation, *Chem. Eng. J.*, 2019, **356**, 393–399.
44 I. Spanopoulos, P. Xydias, C. D. Malliakas and P. N. Trikalitis, A straight forward route for the development of metal-organic frameworks functionalized with aromatic –OH groups: synthesis, characterization, and gas (N2, Ar, H2,

CO2, CH4, NH3) sorption properties, *Inorg. Chem.*, 2013, **52**, 855–862.

45 S. Bhowal and A. Ghosh, Highly selective fluorescent turn-on-off sensing of OH^-, Al3+ and Fe3+ ions by tuning ESIPT in metal organic frameworks and mitochondria targeted bio-imaging, *RSC Adv.*, 2021, **11**, 27787–27800.

46 H. M. N. Pham, A. V. N. Phan, A. N. T. Phan, V. P. Nguyen, K. M. V. Nguyen, H. N. Nguyen, T. M. Nguyen and M. V. Nguyen, Engineering of efficient functionalization in a zirconium-hydroxyl-based metal-organic framework for ultra-high adsorption of Pb2+ ion from an aqueous medium: an elucidated uptake mechanism, *Mater. Adv.*, 2024, **5**, 5118–5133.

47 X. Wang and Y. Li, Nanoporous carbons derived from MOFs as metal-free catalysts for selective aerobic oxidations, *J. Mater. Chem. A*, 2016, **4**, 5247–5257.

48 X. Luo, L. Ding and J. Luo, Adsorptive removal of Pb(II) ions from aqueous samples with amino-functionalization of metal-organic frameworks MIL-101-Cr, *J. Chem. Eng. Data*, 2015, **60**, 1732–1743.

49 H. Zhang, Y.-H. Luo, F.-Y. Chen, W.-Y. Geng, X.-X. Lu and D.-E. Zhang, Enhancing the spatial separation of photogenerated charges on Fe-based MOFs *via* structural regulation for highly-efficient photocatalytic Cr(VI) reduction, *J. Hazard. Mater.*, 2023, **441**, 129875.

50 Y. He, W. Dong, X. Li, D. Wang, Q. Yang, P. Deng and J. Huang, Modified MIL-100(Fe) for enhanced photocatalytic degradation of tetracycline under visible-light irradiation, *J. Colloid Interface Sci.*, 2020, **574**, 364–376.

51 C. Ma, H. T. Wolterbeek, A. G. Denkova and P. S. Crespo, Porphyrinic metal-organic frameworks as molybdenum adsorbents for the $^{99}Mo/^{99m}Tc$ generator, *Inorg. Chem. Front.*, 2023, **10**, 2239–2249.

52 L. Leonat, S. B. Gabriela and I. V. Brañzoi, Cyclic voltammetry for energy levels estimation of organic materials, *UPB Sci. Bull. Ser. B*, 2013, **75**, 111–118.

53 J. Gong, Y. Tang, H. Yang and P. Yang, Theoretical investigations of sp–sp^2 hybridized capped graphyne nanotubes, *Chem. Eng. Sci.*, 2015, **134**, 217–221.

54 Y. Huang, W. Fan, B. Long, H. Li, F. Zhao, Z. Liu, Y. Tong and H. Ji, Visible light $Bi_2S_3/Bi_2O_3/Bi_2O_2CO_3$ photocatalyst for effective degradation of organic pollutions, *Appl. Catal., B*, 2016, **185**, 68–76.

55 A. Gomez-Aviles, M. Penas-Garzon, J. Bedia, D. D. Dionysiou, J. J. Rodriguez and C. Belver, Mixed Ti-Zr metal-organic frameworks for the photodegradation of acetaminophen under solar irradiation, *Appl. Catal., B*, 2019, **253**, 253–262.

56 D. He, H. Niu, S. He, L. Mao, Y. Cai and Y. Liang, Strengthened Fenton degradation of phenol catalyzed by core/shell Fe-Pd@C nanocomposites derived from mechanochemically synthesized Fe-Metal organic frameworks, *Water Res.*, 2019, **162**, 151–160.

57 C. Yao, Y. Xu and Z. Xia, A carbon dot-encapsulated UiO-type metal organic framework as a multifunctional fluorescent sensor for temperature, metal ion and pH detection, *J. Mater. Chem. C*, 2018, **6**, 4396–4399.

58 W. Yan, Y. Yu, H. Zou, X. Wang, P. Li, W. Gao, J. Wang, S. Wu and K. Ding, Promoted photocatalytic hydrogen evolution by molecular ring-substituting doping and regulation of charge carrier migration in graphitic carbon nitride, *Sol. RRL*, 2018, **2**, 1800058.

59 N. Sharma, A. K. Dey, R. Y. Sathe, A. Kumar, V. Krishnan, T. D. Kumar and C. M. Nagaraja, Highly efficient visible-light-driven reduction of Cr(VI) from water by porphyrin-based metal-organic frameworks: effect of band gap engineering on the photocatalytic activity, *Catal. Sci. Technol.*, 2020, **10**, 7724–7733.

60 D. Yang, Y. Sun, Z. Tong, Y. Nan and Z. Jiang, Fabrication of bimodal-pore $SrTiO_3$ microspheres with excellent photocatalytic performance for Cr(VI) reduction under simulated sunlight, *J. Hazard. Mater.*, 2016, **312**, 45–54.

61 Y. Li, Y. Bian, H. Qin, Y. Zhang and Z. Bian, Photocatalytic reduction behavior of hexavalent chromium on hydroxyl modified titanium dioxide, *Appl. Catal., B*, 2017, **206**, 293–299.

62 H. Li and L. Zhang, Oxygen vacancy induced selective silver deposition on the {001} facets of BiOCl single-crystalline nanosheets for enhanced Cr(VI) and sodium pentachlorophenate removal under visible light, *Nanoscale*, 2014, **6**, 7805–7810.

63 R. Liang, F. Jing, L. Shen, N. Qin and L. Wu, MIL-53(Fe) as a highly efficient bifunctional photocatalyst for the simultaneous reduction of Cr(VI) and oxidation of dyes, *J. Hazard. Mater.*, 2015, **287**, 364–372.

64 Q. Liu, C. Zeng, L. Ai, Z. Hao and J. Jiang, Boosting visible light photoreactivity of photoactive metal-organic framework: Designed plasmonic Z-scheme Ag/AgCl@MIL-53-Fe, *Appl. Catal., B*, 2018, **224**, 38–45.

65 X.-H. Yi, S.-Q. Ma, X.-D. Du, C. Zhao, H. Fu, P. Wang and C.-C. Wang, The facile fabrication of 2D/3D Z-scheme g-C_3N_4/UiO-66 heterojunction with enhanced photocatalytic Cr(VI) reduction performance under white light, *Chem. Eng. J.*, 2019, **375**, 121944.

66 X.-D. Du, X.-H. Yi, P. Wang, W. Zheng, J. Deng and C.-C. Wang, Robust photocatalytic reduction of Cr(VI) on UiO-66-NH_2(Zr/Hf) metal-organic framework membrane under sunlight irradiation, *Chem. Eng. J.*, 2019, **356**, 393–399.

67 L. Shi, T. Wang, H. Zhang, K. Chang, X. Meng, H. Liu and J. Ye, An amine-functionalized iron(III) metal-organic framework as efficient visible-light photocatalyst for Cr(VI) reduction, *Adv. Sci.*, 2015, **2**, 1500006.

68 L. Shen, L. Huang, S. Liang, R. Liang, N. Qin and L. Wu, Electrostatically derived self-assembly of NH_2-mediated zirconium MOFs with graphene for photocatalytic reduction of Cr(VI), *RSC Adv.*, 2014, **4**, 2546–2549.

69 H. Li, C. Zhao, X. Li, H. Fu, Z. Wang and C.-C. Wang, Boosted photocatalytic Cr(VI) reduction over Z-scheme MIL-53(Fe)/$Bi_{12}O_{17}Cl_2$ composites under white light, *J. Alloys Compd.*, 2020, **844**, 156147.

70 D. Pattappan, K. V. Kavya, S. Vargheese, R. T. R. Kumar and Y. Haldorai, Graphitic carbon nitride/NH_2-MIL-101(Fe) composite for environmental remediation: visible-light-assisted

photocatalytic degradation of acetaminophen and reduction of hexavalent chromium, *Chemosphere*, 2022, **286**, 131875.

71 A. A. Oladipo, MIL-53(Fe)-based photo-sensitive composite for degradation of organochlorinated herbicide and enhanced reduction of Cr(VI), *Process Saf. Environ. Prot.*, 2018, **116**, 413–423.

72 N. Sharma, A. K. Dey, R. Y. Sathe, A. Kumar, V. Krishnan, T. J. D. Kumar and C. M. Nagaraja, Highly efficient visible-light-driven reduction of Cr(VI) from water by porphyrin-based metal–organic frameworks: effect of band gap engineering on the photocatalytic activity, *Catal. Sci. Technol.*, 2020, **10**, 7724–7733.

73 B. Valizadeh, T. N. Nguyen, S. Kampouri, D. T. Sun, M. D. Mensi, K. Stylianou, B. Smit and W. L. Queen, A novel integrated Cr(VI) adsorption–photoreduction system using MOF@ polymer composite beads, *J. Mater. Chem. A*, 2020, **8**, 9629–9637.

74 J. Gong, Y. Tang, H. Yang and P. Yang, Theoretical investigations of sp–sp^2 hybridized capped graphyne nanotubes, *Chem. Eng. Sci.*, 2015, **134**, 217–221.

75 N. Sharma, A. K. Dey, R. Y. Sathe, A. Kumar, V. Krishnan, T. J. D. Kumar and C. M. Nagaraja, Highly efficient visible-light-driven reduction of Cr(VI) from water by porphyrin-based metal–organic frameworks: effect of band gap engineering on the photocatalytic activity, *Catal. Sci. Technol.*, 2020, **10**, 7724–7733.

76 F. Wang, R. Xue, Y. Ma, Y. Ge, Z. Wang, X. Qiao and P. Zhou, Study on the performance of a MOF-808-based photocatalyst prepared by a microwave-assisted method for the degradation of antibiotics, *RSC Adv.*, 2021, **11**, 32955–32964.